ADVANCED FUNCTIONAL MATERIALS
www.afm-journal.de

Nanoscale Agglomeration Mechanisms of BF-DPB:BPyMPM Donor–Acceptor Systems for Organic Optoelectronic Devices

*Milena Merkel, Philipp Wiesener, Robert Schmidt, Rishi Shivhare, Nikos Doltsinis, Rudolf Bratschitsch, Saeed Amirjalayer, Koen Vandewal, and Harry Mönig**

The molecular order of the photo-active molecules in organic solar cells and exciplex organic light emitting diodes based on donor–acceptor mixed systems has major influence on the performance. However, it is usually investigated only by indirect measurements or simulations. Here, low-temperature scanning probe microscopy is used to directly image the molecular assembly, intermolecular bonding configuration, and domain interfaces of vacuum-deposited donor and acceptor molecules BF-DPB and BPyMPM on different single crystalline substrates with submolecular resolution. It is demonstrated that the position of the nitrogen atoms in the peripheric pyridine rings of BPyMPM molecules determines the occurrence of intermolecular C—H...N hydrogen bonds, metal coordination bonds, and related self-assemblies. Two dominating self-assembled structures of BF-DPB are found, based either on its cis or trans configuration. In general a distinct increase in disorder occurs at the BF-DPB:BPyMPM interface where scanning tunneling spectroscopy indicate an increase in the HOMO-LUMO gap at disordered agglomerates of BF-DPB. The crucial effect of the choice of substrate on the molecular order is illustrated. Photoluminescence measurements indicate a considerable increase in intersystem crossing in BF-DPB due to molecule-substrate interactions. These findings provide new insights for the targeted molecular design of active molecules and suitable contact layers in organic optoelectronic devices.

1. Introduction

Minor changes in the molecular structure of the donor or acceptor molecules of organic solar cells can lead to major differences in solar cell properties.[1,2] The molecular structure determines the molecular order, which has a strong influence on light absorption, mixing of donor and acceptor materials in the bulk heterojunction, exciton splitting, charge transport efficiency, and ultimately on the device power conversion efficiency (PCE).[3–6] For example, it has been shown in the literature for various donor and acceptor molecules that intermolecular hydrogen bonds lead to self-organized layers and subsequent stacking of these layers. In the vast majority of cases, this increased order leads to improved charge transport and higher device performance.[7] Consequently, molecular engineering is often used to improve the molecular order and thus the macroscopic properties of the solar cell.[8,9] However, the molecular order is usually only determined by simulations or indirect measurements, such as absorption measurements or grazing-incidence wide-angle X-ray scattering (GIWAXS).[10,11] Using high-resolution scanning probe microscopy (SPM) allows to directly image the molecular order in real space and to identify intermolecular order mechanisms and their correlation with the optoelectronic properties. This can help to gain a fundamental understanding of the relationship between molecular order and

M. Merkel, P. Wiesener, R. Schmidt, R. Bratschitsch, H. Mönig
Physikalisches Institut
Universität Münster
Wilhelm-Klemm-Strasse 10, 48149 Münster, Germany
E-mail: harry.moenig@uni-muenster.de
M. Merkel, P. Wiesener, H. Mönig
Center for Nanotechnology
Heisenbergstrasse 11, 48149 Münster, Germany

DOI: 10.1002/adfm.202420307

R. Shivhare, K. Vandewal
Institute for Materials Research (imo-imomec)
Hasselt University
Martelarenlaan 42, Hasselt B-3500, Belgium
R. Shivhare, K. Vandewal
imec
imo-imomec
Wetenschapspark 1, Diepenbeek B-3590, Belgium
N. Doltsinis
Institut für Festkörpertheorie
Universität Münster
Wilhelm-Klemm-Strasse 10, 48149 Münster, Germany
S. Amirjalayer
Interdisciplinary Center for Scientific Computing
Universität Heidelberg
Im Neuenheimer Feld 205A, 69120 Heidelberg, Germany

BF-DPB (donor)	B2PyMPM (acceptor)	B3PyMPM (acceptor)	B4PyMPM (acceptor)
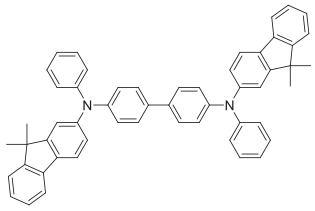	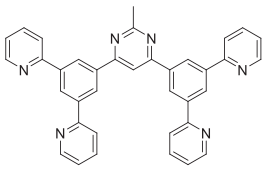	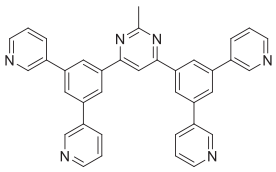	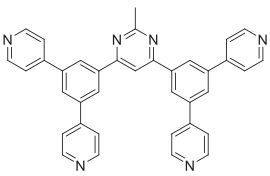
Electron mobilities [$cm^2 V^{-1} s^{-1}$] [10]	1.6×10^{-6}	1.5×10^{-5}	1.0×10^{-4}
In BF-DPB:BxPyMPM blends [11]:			
CT states	Strongly bound	Strongly bound	Unbound
Charge carrier generation	Inefficient and strongly electric field-dependent	Inefficient and electric field-dependent	Efficient and electric field-independent
Photovoltaic FF [%]	19.1	35.0	72.0

Figure 1. Chemical structures and device performance data of BF-DPB, B2PyMPM, B3PyMPM and B4PyMPM molecules. The device performance data are taken from Refs. [10] and [11].

PCE and pave the way for further, knowledge based material engineering.

Here, we show the potential of scanning tunneling microscopy (STM) for molecular order determination on the interesting system of BF-DPB:BPyMPM donor–acceptor blends. Usually, the organic semiconductor blends that are best suited for organic light-emitting diodes (OLEDs) are different from those that are best suited for organic solar cells (OSCs). Accordingly, the donor–acceptor combination of BF-DPB and B4PyMPM stands out as it exhibits both efficient photogeneration of free charge carriers and a high electroluminescence quantum yield and can therefore be successfully applied in both OLEDs and OSCs.[12,13] BF-DPB was originally only used as a hole transport material, but later also proved to be a highly suitable donor material.[14–17] Due to the high energy gap of both BF-DPB and B4PyMPM, the corresponding OLEDs emit in the visible range, while the corresponding OSCs absorb in the blue to UV range.[17,18] This absorption range is far from the optimum defined by the Shockley-Queisser limit, leading to a low short-circuit current density in BF-DPB:B4PyMPM solar cells.[13] However, BF-DPB:B4PyMPM blends have potential in building-integrated applications or multi-junction solar cells.[17,19]

A major disadvantage of organic solar cells compared to their inorganic counterparts is generally their strong non-radiative charge-transfer state decay.[12] It is responsible for significant voltage losses and thus for a low open-circuit voltage (V_{oc}). However, it has been shown that BF-DPB:B4PyMPM solar cells exhibit voltage losses of only 0.45 eV compared to typical values of 0.60 eV in organic solar cells.[12] This is due to their high charge-transfer energy E_{CT}, which reduces the energy coupling to the ground state. Therefore, exceptionally low non-radiative decay occurs, leading to low voltage losses and a high V_{oc} in BF-DPB:B4PyMPM solar cells.[12] Furthermore, in BF-DPB:B4PyMPM devices, the charge transfer states are not strongly bound, leading to efficient free charge carrier generation and thus high fill factors (FF).[12] Previous investigations, in which B4PyMPM is compared with two similar acceptor molecules, B2PyMPM and B3PyMPM, shed some light on the structural cause of this low CT binding energy.[10]

The three molecules B2PyMPM, B3PyMPM, and B4PyMPM have almost the same molecular structure, apart from the position of the nitrogen atoms in their peripheral pyridine rings, see **Figure 1**. However, they differ in their macroscopic physical properties.[10] B4PyMPM has an electron mobility 10 times higher than B3PyMPM and even 100 times higher than B2PyMPM. Additionally, solar cells with B4PyMPM as the acceptor exhibit a much higher fill factor than those with B3PyMPM or B2PyMPM as the acceptor. Based on ellipsometry, UV–vis absorption measurements, X-ray diffraction measurements and quantum calculations, Yokoyama et al. stated that the molecules in both B3PyMPM films and B4PyMPM films are mostly aligned parallel to the substrate, with a face-on orientation.[10] In B4PyMPM films, this face-on orientation is even stronger than in B3PyMPM films.[11,20] The reason for the face-on orientation is suggested to be the C—H...N hydrogen bonds between neighboring molecules that induce the formation of 2D molecular networks, which then stack on top of each other in form of molecular planes.[10] This molecular stacking allegedly induces the high electron mobility in B4PyMPM. Additionally, the high order could lead to a more delocalized charge-transfer state. Therefore, its binding energy is lower, which enables more efficient free charge carrier generation and thus a high FF, especially in B4PyMPM-based solar cells.[11,18] B2PyMPM molecules, on the other hand, cannot form C—H...N hydrogen bonds with

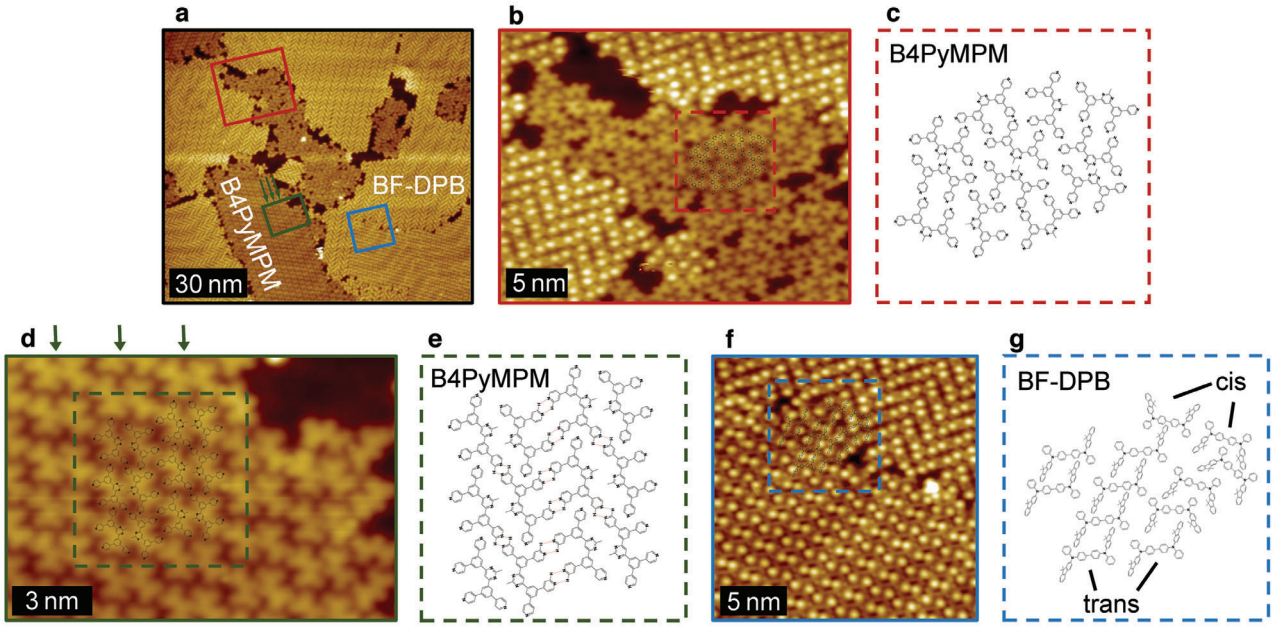

Figure 2. B4PyMPM and BF-DPB molecules evaporated consecutively on a Au(111) surface. a) Overview STM image of different molecular assemblies of B4PyMPM and BF-DPB. The rows of the B4PyMPM molecular assembly are indicated by green arrows. b) STM image of a disordered domain of B4PyMPM. c) Magnified scheme of the molecular assembly in (b). d) STM image of the ordered domain of B4PyMPM. The rows of the molecular assembly are indicated by green arrows. e) Magnified scheme of the molecular assembly in (d) with C–H...N hydrogen bonds in red. f) STM image of the BF-DPB cis and trans configuration domains. g) Magnified scheme of the molecular assembly in (f). All STM images were taken with voltage and tunneling current setpoints of 2.5 V and 10 pA. B4PyMPM was evaporated for 20 min, then BF-DPB for 5 min.

neighboring molecules due to steric hindrance. Therefore, B2PyMPM films allegedly remain amorphous with isotropically oriented molecules, resulting in localized charge-transfer states, a high CT binding energy and a low FF.[11]

Given that the photon absorption, exciton splitting and charge transport efficiency of organic solar cells are drastically affected by the nanoscale configuration of the donor/ acceptor domains and interfaces, scanning probe microscopy studies can help to correlate the microscopic structure with the macroscopic device properties.[21–23] In the present study we use low-temperature scanning probe microscopy with submolecular resolution to study the fundamental agglomeration mechanisms and intermolecular bonding configurations of the BF-DPB donor and BPyMPM acceptor molecules under well defined conditions. We image the 2D molecular assembly of vacuum-deposited BF-DPB and BPyMPM molecules on single crystalline substrates, which is determined by a subtle balance between intermolecular and molecule-substrate interaction. Furthermore, we investigate the change in molecular order and band gap at the BF-DPB:B4PyMPM interface as well as the effect of the substrate on the optical properties of BF-DPB. The corresponding results can help to obtain more information about desirable properties for molecules employed in optoelectronic devices.

2. Results and Discussion

2.1. B4PyMPM and BF-DPB on Au(111)

In order to gain insights into the 2D molecular assembly of B4PyMPM and BF-DPB, the two molecules were deposited on a clean Au(111) surface by sequential evaporation as well as co-evaporation under ultra-high vacuum (UHV) and studied using scanning tunneling microscopy and scanning tunneling spectroscopy (STS). In addition, the molecular structures of an additional second monolayer of B4PyMPM and of a BF-DPB layer on a monolayer of B4PyMPM were investigated to gain knowledge about the bulk properties.

2.1.1. Sequential Evaporation

After sequential evaporation of B4PyMPM and BF-DPB, the subsequent STM analysis shows that the two molecules are adsorbed on the Au(111) surface, creating a monolayer (ML) made of differently sized domains of either B4PyMPM or BF-DPB (**Figure 2a**).

The B4PyMPM molecules form both disordered (Figure 2b,c) and ordered domains (Figure 2d,e). In the disordered domains the molecules are randomly oriented, suggesting that only van der Waals interaction occurs between the individual molecules. In the ordered domains, however, the molecules are arranged in rows of two B4PyMPM facing each other, as indicated by the green arrows in Figure 2a,d. Submolecular analysis shows that every nitrogen atom in the peripheral pyridine rings is facing a hydrogen atom in a neighboring molecule. This suggests intramolecular C–H...N hydrogen bonds in addition to the van der Waals forces. The H...N bond length between the B4PyMPM molecules is (232 ± 51) pm and therefore lies in the typical range of hydrogen bond lengths in molecular films on metal substrates.[24–26] Such a molecular assembly caused by hydrogen bonds matches previous predictions well.[10]

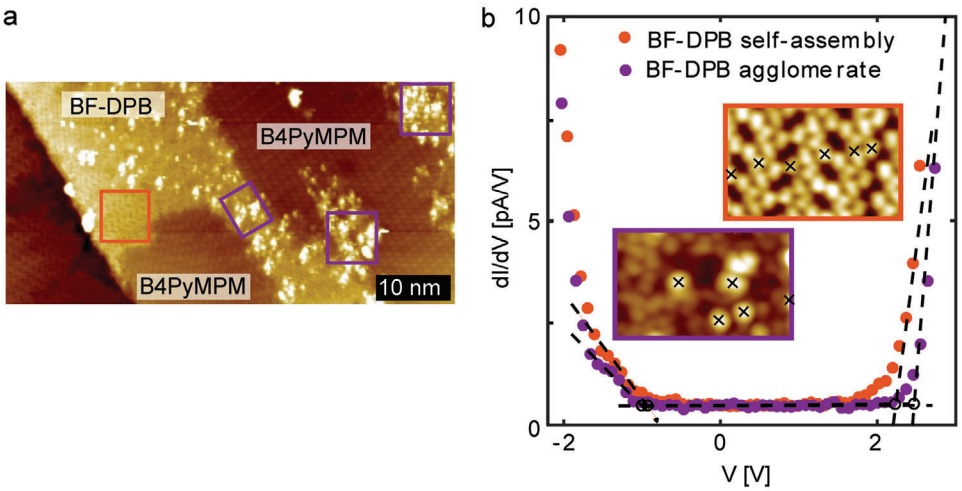

Figure 3. Band gap estimation. a) Overview STM image of a BF-DPB self-assembly (highlighted by orange square) and BF-DPB agglomerates (highlighted by purple squares) next to a B4PyMPM self-assembly. b) Scanning tunneling spectroscopy of a BF-DPB self-assembly and BF-DPB agglomerates. The individual measurement positions are marked by crosses in the insets. The width of the insets is 10 nm. Dashed aid lines added for band gap estimation. B4PyMPM was evaporated for 20 min, then BF-DPB for 10 min.

The BF-DPB molecules adsorb on the Au(111) either in cis or trans configuration and form larger self-assemblies consisting exclusively of one of these two configurations (Figure 2f,g). These self-assemblies make up about 95 % of BF-DPB domains and thus represent the standard morphology. They are determined by van der Waals interaction between neighboring molecules and molecule-substrate interactions. In the cis configuration, the larger side groups are on the same side of the molecule, whereas in the trans configuration, they are on opposite sides. The brighter appearance of these side groups in the STM images indicates that they are tilted out of plane. Both self-assemblies, the one consisting of molecules in cis configuration and the one consisting of molecules in trans configuration, exhibit a density of about 0.4 molecules/nm^2 . Self-assemblies made of a combination of the two configurations are not found, presumably because they would form less dense layers. Voids are formed at the interfaces between areas of different configurations, indicating that the two configurations cannot form a continuous layer together (Figure 2f).

In addition to ordered self-assemblies, BF-DPB molecules also form disordered agglomerates (**Figure 3**a). They are mainly found at interfaces with B4PyMPM and when space is limited. In these cases, the molecules tilt out of the plane and 3D islands are formed. Scanning tunneling spectroscopy current–voltage curves are measured both on these agglomerates and on BF-DPB molecules in the self-assembled structure. By numerical differentiation of the current–voltage curves, dI/dV curves are obtained that are proportional to the density of states of the molecules (Figure 3b). They can therefore be used to estimate the bandgap of the molecules. For this purpose, the intersection points of the linear fits of the bandgap and the rising sides of the curve corresponding to the HOMO and the LUMO are determined. The agglomerated BF-DPB molecules have an approximately 0.3 eV higher bandgap than the BF-DPB molecules in a self-assembly. While the absolute values for the bandgap vary depending on the exact configuration of the tip, only the relative changes between measurements made with an identical tip are considered here.[27]

A common theory regarding charge generation in OSCs is that efficient charge carrier separation requires a large energy offset between the lowest excited singlet state and the charge transfer state, which limits the achievable PCE.[28] However, this is not the case for all donor–acceptor combinations. Some exhibit an efficient charge carrier separation despite a small energy offset.[29] For these materials, it was hypothesized that the spatial separation of photogenerated charges is driven by an energy relaxation due to the cascading energy levels, being more favorable for the charge carriers to reside in the more ordered domains at larger distances from the donor–acceptor interface.[29,30] This hypothesis is corroborated by our results, which show a reduction of order at the BF-DPB:B4PyMPM interface along with a higher band gap. The lower energy gap in the ordered area could subsequently direct holes in BF-DPB away from the interface, leading to the dissociation of bound into free charge carriers.

2.1.2. Co-evaporation

Next, B4PyMPM and BF-DPB were evaporated simultaneously on Au(111). The two molecules barely mix and instead rather form bigger domains with varying width in the range of about 5 nm to 60 nm consisting of only one of the molecules (**Figure 4**). Such a formation of domains of the donor and acceptor materials is advantageous in a solar cell bulk heterojunction to achieve both facile exciton separation at the donor–acceptor interface and sufficient charge carrier extraction at the electrodes. Domain sizes that roughly correspond to the exciton diffusion length, which is typically in the range of 5 nm - 10 nm for organic semiconductors, are optimal.[31,32]

The formation of these well-defined, separate B4PyMPM and BF-DPB domains is most likely caused by the very different

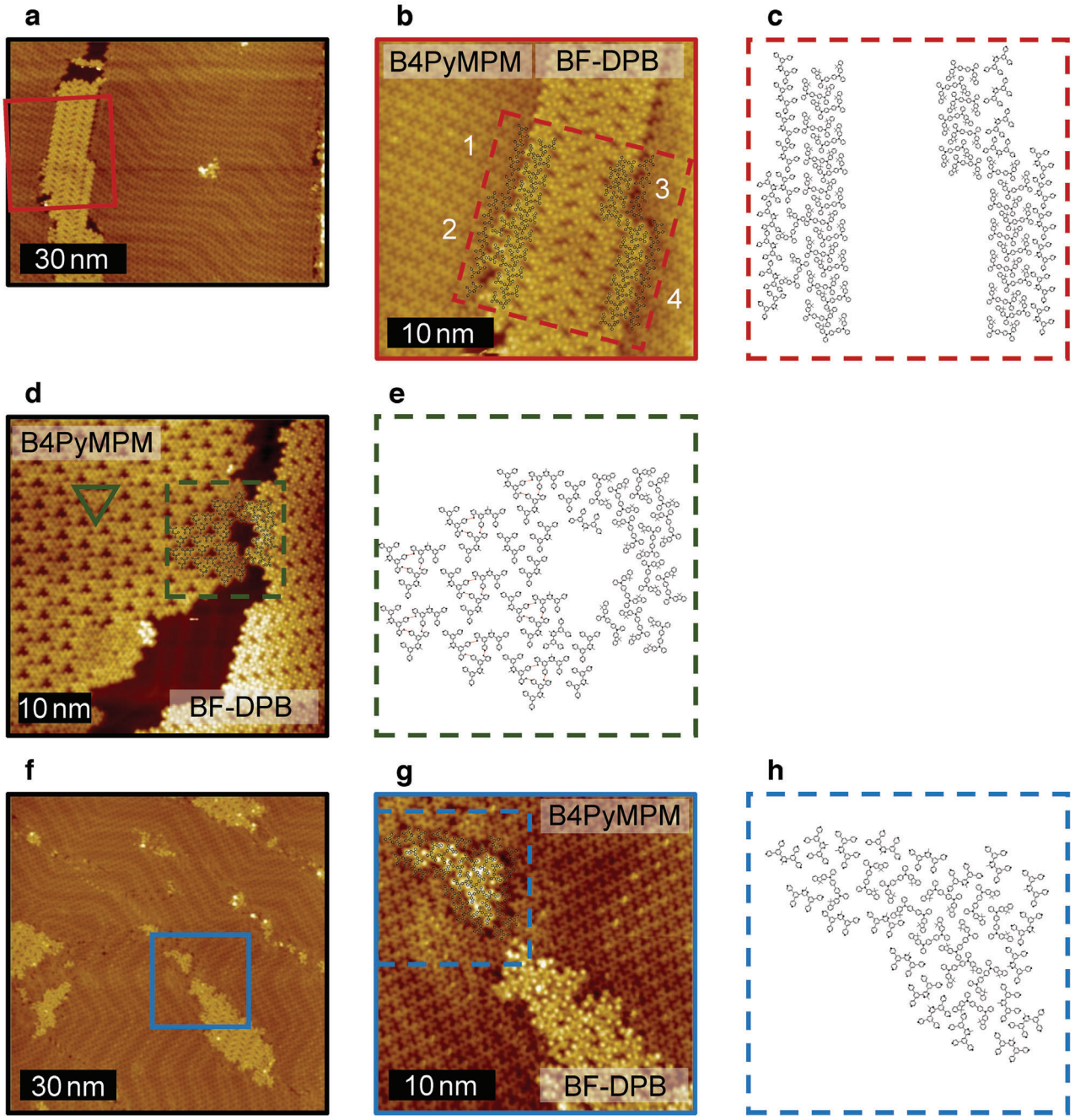

Figure 4. B4PyMPM and BF-DPB molecules evaporated simultaneously on a Au(111) surface. a) Overview STM image of the interface of B4PyMPM and BF-DPB domains. b) STM image of an interface segment in (a) with four different relative orientations of B4PyMPM versus BF-DPB. c) Magnified scheme of the molecular assembly at the B4PyMPM:BF-DPB interface in (b). d) STM image of the B4PyMPM self-assembly with triangular unit cell (marked with a green triangle) next to a BF-DPB domain. e) Magnified scheme of the molecular assembly at the B4PyMPM:BF-DPB interface in (d) with C–H...N hydrogen bonds in red. f) Overview STM image of the interface of B4PyMPM and BF-DPB domains after annealing up to 180 °C. g) STM image of an interface segment in (f). h) Magnified scheme of the molecular assembly at the B4PyMPM:BF-DPB interface in g). All STM images were taken with voltage and tunneling current setpoints of 2.5 V and 10 pA. B4PyMPM and BF-DPB were co-evaporated for 7 min.

intermolecular interactions and distinct adsorption geometries of these two molecules. While the assembly of B4PyMPM is dominated by hydrogen bonding in a flat adsorption geometry, BF-DPB interacts by considerably weaker van der Waals interactions in conjunction with pronounced out-of-plane rotated aromatic units (Figure S1, Supporting Information). At the same time, hydrogen bonds between BF-DPB and B4PyMPM are prevented by the difference in height and unfavorable directionality of their peripheral atoms (Figure S1, Supporting Information). As a result, the B4PyMPM network based on hydrogen bonds is

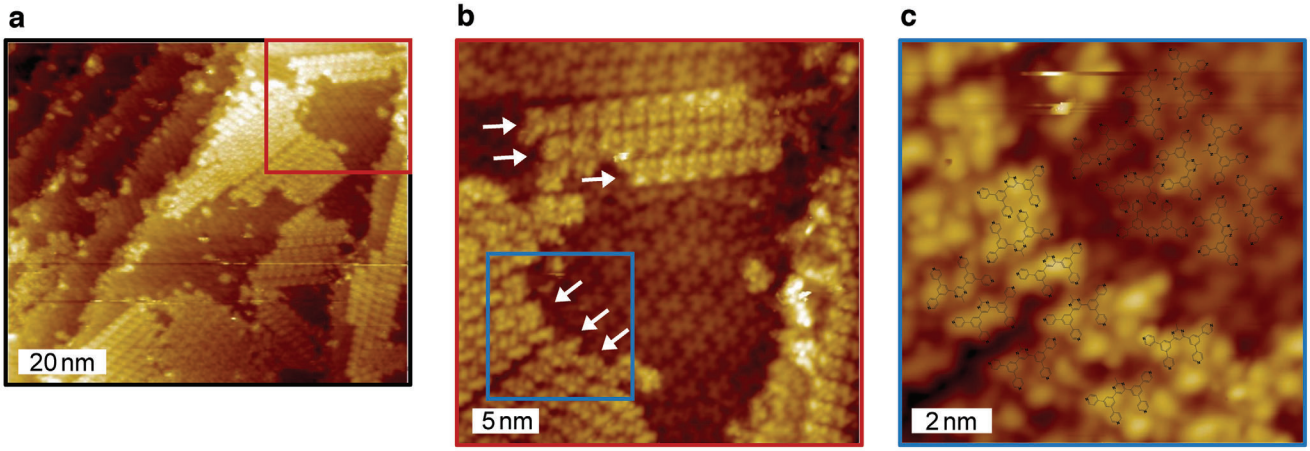

Figure 5. 1.5 MLs B4PyMPM on a Au(111) surface. a) Overview STM image (1.2 V, 5 pA). b) Enlarged STM image containing areas with both 1 ML and 2 MLs of B4PyMPM (1.2 V, 5 pA). Ordered rows in the second ML are indicated by white arrows. c) High resolution image with scheme of the molecular assembly (1.0 V, 5 pA). B4PyMPM was evaporated for 100 min.

energetically preferred, which prevents blending with BF-DPB. Consequently, using an acceptor molecule without the capability to form strong hydrogen bonds should show a higher tendency to blend with the BF-DPB donor. STM measurements of B2PyMPM and BF-DPB molecules co-evaporated on a Au(111) surface confirm this trend (Figure S2, Supporting Information). At low coverage, the BF-DPB molecules form elongated clusters confined by the Au(111) herringbone reconstruction (Figure S2a, Supporting Information). In contrast, the co-evaporated B2PyMPM molecules appear highly mobile, resulting in unstable imaging conditions. At a coverage close to a monolayer (Figure S2b, Supporting Information), the typical BF-DPB structures (Figure 2) are dissolved. Instead, a disordered assembly is observed where B2PyMPM molecules are integrated into the BF-DPB layer. Such a strong intermixing of the acceptor and donor molecules is disadvantageous in a BHJ, as separated charge carriers then easily recombine before reaching the electrodes. Since rapid charge carrier recombination leads to lower FFs, this strong mixing may be a reason for the inferior FFs of B2PyMPM:BF-DPB cells compared to B4PyMPM:BF-DPB cells (see Figure 1). Since the main difference between B4PyMPM and B2PyMPM lies in the lack of hydrogen bonds between B2PyMPM molecules, this indicates that the hydrogen bonds and related strong intermolecular interaction between neighboring B4PyMPM molecules induce the phase segregation with BF-DPB leading to well-defined, separate B4PyMPM and BF-DPB domains. This is in line with standard thermodynamic arguments for demixing phenomena, which can be explained by a large difference between the cohesive energy densities of the two substances.[33] Further measurements of B2PyMPM individually evaporated on Au(111) and Cu(111) are discussed in Sections 2.3 and 2.5.

The interface between B4PyMPM and BF-DPB domains is not uniform (Figure 4a–c). While the domains are largely ordered within themselves, this order is disturbed at the interfaces and the molecules are partially rotated in the plane (Figure 4b). However, this does not result in a uniform orientation of BF-DPB and B4PyMPM molecules to each other, but many different ones (four different ones shown in Figure 4b).

In addition to the rows shown in Figure 2d, B4PyMPM molecules form a second type of self-assembly based on a unit cell of three triangularly aligned molecules (Figure 4d,e). The unit cell is marked as a green triangle in Figure 4d. The nitrogen atoms of one molecule are facing the hydrogen atoms of a neighboring molecule with a distance of (262 ± 41) pm.

Annealing of the molecules on Au(111) up to 180 °C does not lead to a further mixing of the two molecules (Figure 4f–h). Still, B4PyMPM and BF-DPB molecules form mostly ordered domains, while only small domains and interfacial areas are disordered.

2.1.3. B4PyMPM Second Layer Growth

In order to investigate the 3D structural order of B4PyMPM, a sample with 1.5 monolayers of B4PyMPM on Au(111) was prepared (**Figure 5**). Here, the analysis is extremely challenging because the second layer is only weakly bound. It forms ordered rows on top of the first monolayer, marked with white arrows in Figure 5b. The rows of the second layer appear to be aligned parallel to the rows of the first layer. Most likely, this trend continues below the second layer. Additionally, the first layer is partially disordered in lateral proximity to the second layer, which may have induced the growth of the second layer at this location. Furthermore, the STM contrast indicates that the second layer is slightly tilted out of plane, resulting in a non-flat molecular configuration. In corresponding devices, this stacking of ordered molecular planes leads to a high electron mobility and delocalized CT states and thus to efficient, field-independent charge carrier generation and a high FF.[10,11]

2.1.4. BF-DPB on B4PyMPM

In a complete device, charge transport takes place in vertical direction and not through horizontal van der Waals interactions or hydrogen bonds. The exciton dissociation also occurs at the horizontal interface of the stacked donor and acceptor layers.

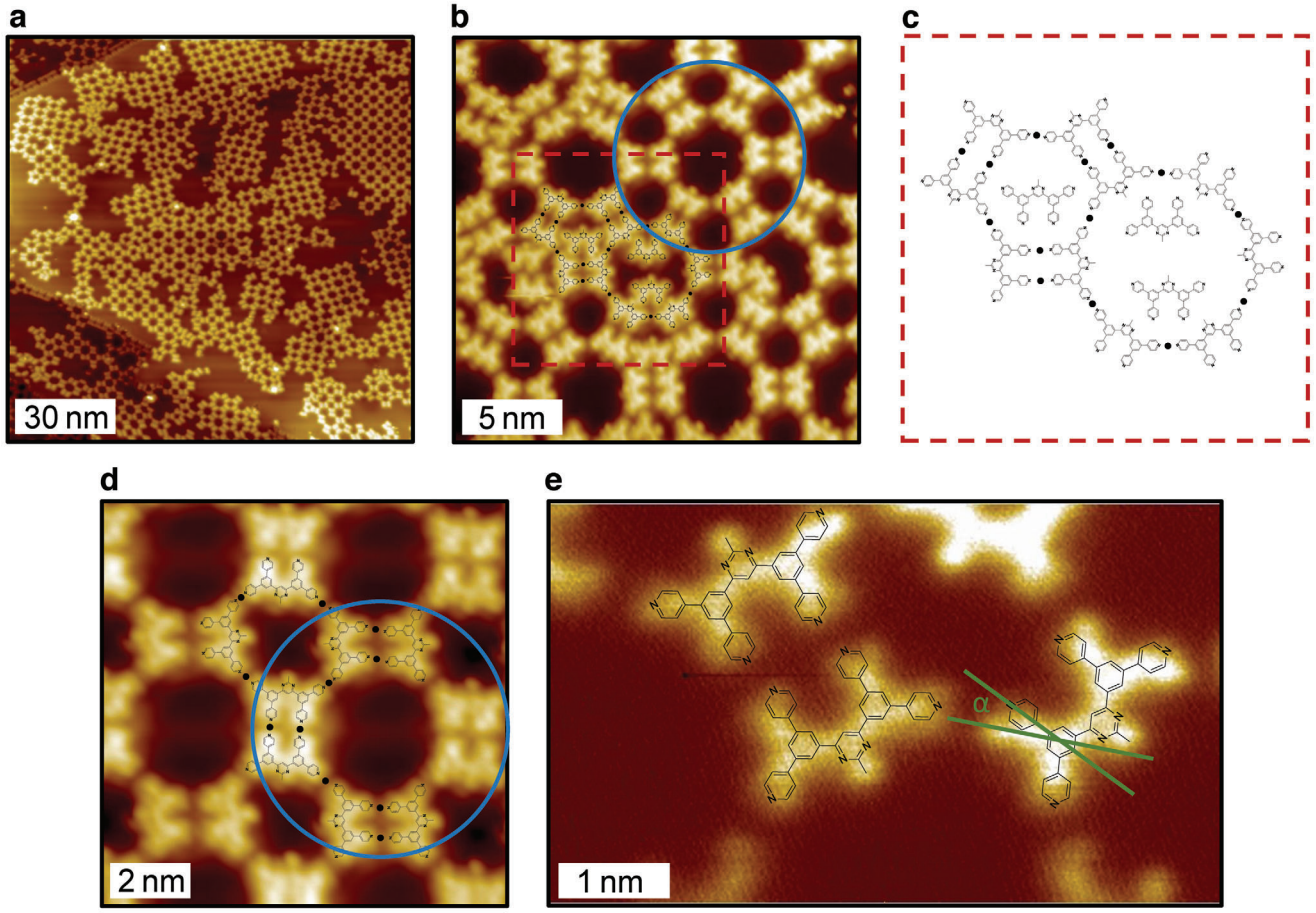

Figure 6. B4PyMPM on a Cu(111) surface with metal coordination bonds shown as dots. a) Overview STM image (−2.0 V, 10 pA). b) STM image of self-assembly with hexagonal symmetry (−0.7 V, 50 pA). Unit cell marked by blue circle. c) Magnified scheme of molecular assembly of B4PyMPM in (b). d) STM image of self-assembly with square symmetry (−0.7 V, 50 pA). Unit cell marked by blue circle. e) High resolution constant height STM image of disordered region recorded with a qPlus sensor and an oxygen terminated copper tip (0.0 V).[40,41] B4PyMPM molecule bend outwards by $\alpha = 25°$. B4PyMPM was evaporated for 10 min.

Nevertheless, the horizontal 2D assembly of the molecules is highly relevant as it strongly influences layer growth in 3D. To shed more light on the 3D structure, BF-DPB was deposited on a monolayer of B4PyMPM on Au(111) (Figure S3, Supporting Information). BF-DPB forms 3D islands on B4PyMPM, similar to the agglomerates found in lateral vicinity to B4PyMPM (Figure 3). Thus, we can assume that the band gap of BF-DPB at the disordered horizontal interface to B4PyMPM, similar to that at the disordered lateral interface, is higher than in ordered regions, directing the charge carriers away from the interface.

2.2. B4PyMPM on Cu(111)

In order to elucidate the effects of a more reactive substrate on the molecular assembly, B4PyMPM was deposited on a clean Cu(111) surface (**Figure 6**). The reactivity of a metal substrate is determined by the degree of filling of the antibonding states upon adsorption and by the degree of orbital overlap with the adsorbate.[34] Both Au and Cu exhibit a filled antibonding state upon adsorption, making them less reactive than metals such as nickel or platinum. However, Au exhibits a larger degree of orbital overlap with the adsorbate than Cu, which drives up the energy. Therefore, the chemical reactivity of Au(111) is smaller than that of Cu(111).[35] On Cu(111), metal coordination bonds form especially with nitrogen-containing molecules.[36] Two different types of self-assembly are observed on Cu(111), one with hexagonal symmetry (Figure 6b,c) and one with a square symmetry (Figure 6d). In both cases the assemblies are based on dimers of B4PyMPM. The respective unit cells are marked by blue rings in Figure 6b,d. The hexagonal symmetry of the structure in Figure 6b reflects the main symmetry axes of the Cu(111) substrate. In both self-assemblies, the nitrogen atoms in the peripheral pyridine rings of neighboring molecules face each other, indicating metal coordination bonds between these two nitrogen atoms and a central copper atom of the Cu(111) substrate.[37] Metal coordination bonds usually have a length in the range of 150 pm to 250 pm.[38,39] Here, in the case of the structure with hexagonal symmetry, the distance between the nitrogen atom and the central copper atom is (280 ± 30) pm, which indicates a weak metal coordination bond (Figure 6b,c). In the case of the structure with square symmetry, the distance is only (220 ± 30)

pm, indicating a stronger bond. Figure 6e shows that in disordered regions, the peripheral pyridine rings even bend outwards to form a metal coordination bond (here by $\alpha = 25$ °).

2.2.1. Passivation Layers

Both B4PyMPM and BF-DPB were also deposited on a bilayer/trilayer of sodium chloride (NaCl) on top of Cu(111) (Figure S4, Supporting Information). NaCl acts as a decoupling layer to reduce interaction between the molecules and the Cu(111) substrate.[42,43] The BF-DPB molecules agglomerate in form of non-flat islands with a diameter of 4 nm to 6 nm at step edges and domain boundaries of the NaCl (Figure S4a–c, Supporting Information). These islands can be moved by the STM tip, confirming a weak molecule-substrate interaction. The STM contrast suggests a complex 3D agglomeration of the BF-DPB molecules. The B4PyMPM molecules individually assemble at NaCl step edges or in small openings within the NaCl layer and can be moved by the STM tip. Interestingly, they do not form any self-assembled monolayer structures (Figure S4d, Supporting Information). Thus, while B4PyMPM and BF-DPB form self-assembled layers on Au(111) and Cu(111), this is prevented by the chemically passivating layer of NaCl. This shows that a moderate molecule-substrate interaction is required to obtain ordered molecular structures. A second way of passivating the Cu(111) substrate is oxidation. On copper oxide, the BF-DPB molecules agglomerate along rows that follow the orientation of the substrate (Figure S4e, Supporting Information). Copper oxide is also used as a hole transport layer in organic solar cells.[44] However, the analysis is extremely challenging since the BF-DPB molecules are only weakly bound. As shown here and in the previous sections, the molecular assembly and the resulting functional properties are thus highly dependent on the substrate. Therefore, the choice of the contact layers in an organic solar cell is of crucial importance.

2.3. B2PyMPM on Au(111)

B2PyMPM differs from B4PyMPM only in the position of the nitrogen atoms in their peripheral pyridine rings (Figure 1). However, their physical properties vary greatly in macroscopic arrangements, suggesting differences in the molecular assembly of the two molecules.[10,11] For example, as shown in Section 2.1.2, compared to B4PyMPM, B2PyMPM exhibits an increased miscibility with BF-DPB. Here, B2PyMPM was sequentially deposited on a Au(111) surface for different coverages (**Figure 7**). At low coverage, after 3 min and 6 min of thermal evaporation, the B2PyMPM molecules mainly accumulate at the elbows of the herringbone structure of the Au(111) substrate, which are the most reactive sites (Figure 7a,b). The STM contrast of these B2PyMPM islands suggests a 3D molecular configuration. At higher coverage, after 11 min and 14 min of thermal evaporation, the molecules are still partially mobile within a confinement given by the herringbone structure (Figure 7c–e). Additionally, after annealing up to 200 °C, the B2PyMPM molecules remain only at the step edges, leaving the planes empty (Figure 7f). Both indicates a weak molecule-substrate interaction. This is in contrast to the B4PyMPM molecules, which remain on the substrate even after annealing (see Figure 4f,g), possibly due to additional stability provided by the molecular assembly. The B2PyMPM molecules, instead, do not form an ordered self-assembly on Au(111) because the nitrogen atoms in their peripheral pyridine rings are not directed outwards and therefore cannot induce the formation of 2D networks by hydrogen bonding. Such reduced order prevents the stacking of molecular planes in B2PyMPM-based cells, which is the reason for a lower electron mobility, more localized CT states and thus inefficient and strongly electric field-dependent charge carrier generation and a lower photovoltaic FF compared to B4PyMPM-based cells.[10,11]

2.4. B3PyMPM on Au(111)

The third acceptor molecule, B3PyMPM, was also evaporated onto Au(111) (Figure S5, Supporting Information). The nitrogen atoms in its peripheral pyridine rings are in the meta position (see Figure 1). The B3PyMPM molecules form agglomerates on top of a linear pattern, indicating a disordered second layer on top of an ordered first one. Next to the B3PyMPM layers, an empty Au(111) surface remains, signifying a stronger molecule-molecule than molecule-substrate interaction. Even after annealing up to 200 °C, this configuration does not change. Accordingly, the B3PyMPM molecules are more strongly bound to the Au(111) substrate than the B2PyMPM molecules.

2.5. B2PyMPM on Cu(111)

In order to investigate the effect of a more reactive substrate, B2PyMPM is also thermally evaporated on a Cu(111) surface. Interestingly, we observe a disordered structure with nearly equidistant molecules (**Figure 8**a–c). Some molecules appear brighter in the STM image, indicating an out-of-plane tilt in these cases (Figure 8b). Even with high coverage, there is no agglomeration of molecules, indicating a strongly suppressed intermolecular interaction (Figure 8d). In contrast to B4PyMPM, no metal coordination bond can occur between two neighboring molecules and a central copper atom, as the nitrogen atoms in the peripheral pyridine rings of B2PyMPM are not directed outward.

2.6. Photoluminescence Properties of BF-DPB and BF-DPB/B4PyMPM on Au(111)

In addition to the structural investigations using scanning probe microscopy, the optical properties of BF-DPB were studied using photoluminescence (PL) measurements. First, the PL of a BF-DPB powder was measured. It exhibits an emission maximum at 2.80 eV (**Figure 9**). In comparison, the PL maximum of a BF-DPB layer on a Au(111) substrate is strongly redshifted, with an emission maximum at 2.25 eV. The photoluminescence of the Au(111) substrate itself is negligible. The strong PL redshift, going from bulk (powder) to BF-DPB on Au(111), indicates that the

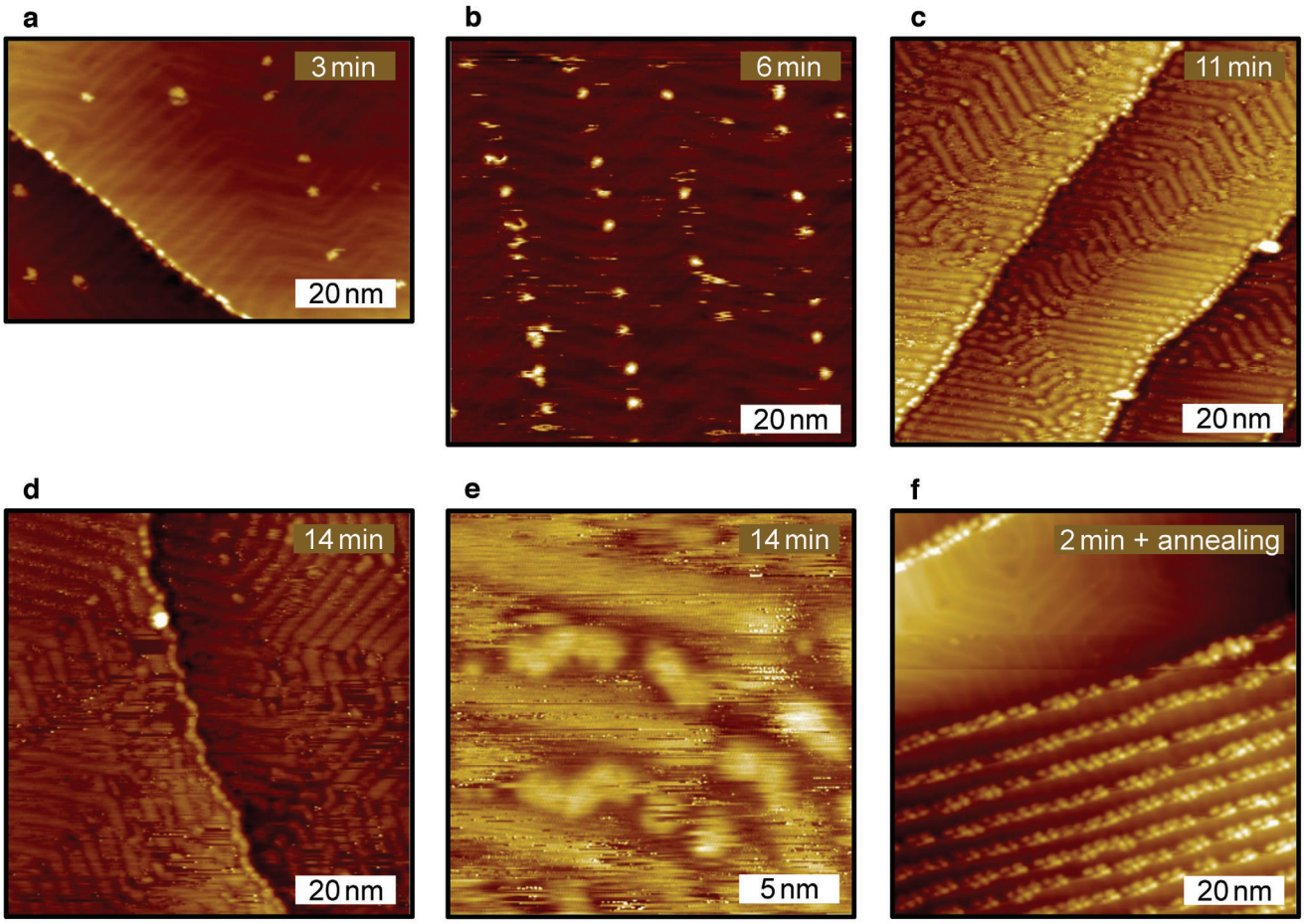

Figure 7. B2PyMPM on a Au(111) surface. a) STM image after 3 min of thermal evaporation (2.6 V, 7 pA). b) STM image after 6 min of thermal evaporation (2.5 V, 7 pA). c) STM image after 11 min of thermal evaporation (2.5 V, 7 pA). d) STM image after 14 min of thermal evaporation (2.5 V, 7 pA). e) Enlarged STM image after 14 min of thermal evaporation (2.5 V, 10 pA). f) STM image after 2 min of thermal evaporation and additional annealing up to 200 °C (2.6 V, 10 pA).

interaction with the Au(111) substrates results in a significant alteration of the optical properties. We relate the observed redshift and broadening of the emission spectrum to a change in the intermolecular forces and molecular configuration of BF-DPB, leading to changes in the excited-state energies of the molecules. In addition, we hypothesize that the close presence of Au(111) results in an enhanced intersystem crossing within BF-DPB, resulting in triplet state population and emission. This is corroborated by DFT calculations of the fluorescence and phosphorescence spectra of BF-DPB in the gas phase (Figure 9). The simulated fluorescence spectrum agrees well with the experimental measurement of the powder spectrum. The calculated position of the peak maximum of the fluorescence spectrum (2.92 eV) shows reasonable agreement with the experimental value of the powder spectrum (2.80 eV). The fact that only fluorescence, i.e., emission from the S_1 singlet state, occurs in the powder can be attributed to the weak spin-orbit coupling in organic compounds. Placing BF-DPB on the Au(111) substrate enables a transition from the S_1 singlet state to the T_1 triplet state by intersystem crossing due to the metal-enhanced spin-orbital coupling. This leads to phosphorescence, i.e., emission from the T_1 state. The simulated phosphorescence maximum is found at 2.38 eV, in good agreement with the experimental maximum of the BF-DPB spectrum on Au(111) (2.25 eV). The theoretical singlet-triplet splitting of 0.54 eV shows excellent agreement with the corresponding difference between the maxima of the powder spectrum and the spectrum on Au(111) (0.55 eV). In practical devices, electron/hole transporting or extraction layers are used in between the photoactive layer and the metal contact, avoiding the undesired metal-enhanced intersystem crossing.

For the samples where BF-DPB was deposited on top of B4PyMPM on Au(111), the PL emission does not change any further. Due to the high energy gap of B4PyMPM, the excitation at 375 nm predominantly excites BF-DPB.[17] In thin films, excitation of BF-DPB:B4PyMPM interfaces results in electron transfer and subsequent emission of the intermolecular charge-transfer (CT) state.[11] We ascribe the lack of CT emission in the BF-DPB/B4PyMPM/Au(111) samples on the strong interactions of the organic components with the Au substrates, favoring a strong redshifted emission from the triplet state, hereby hampering electron transfer from BF-DPB to B4PyMPM and thus the formation of CT states.

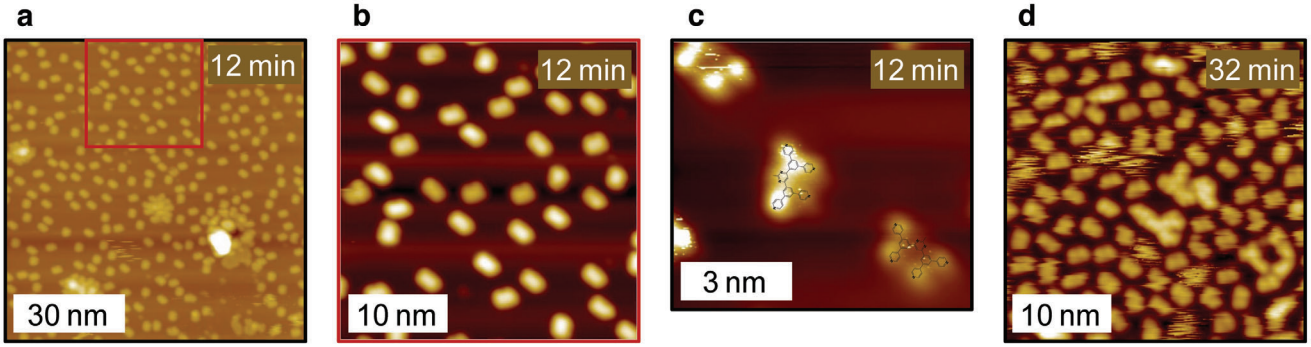

Figure 8. B2PyMPM on a Cu(111) surface. a) Overview STM image after 12 min of thermal evaporation (2.7 V, 10 pA). b) Enlarged STM image of cutout of (a) (2.7 V, 10 pA). c) High resolution constant height current STM image after 12 min of thermal evaporation (0.0 V). d) STM image after 32 min of thermal evaporation (1.0 V, 10 pA).

DFT calculations quantify the binding energy of BF-DPB to the Au(111) substrate to −3.85 eV, which corresponds to a strong physisorption.[45,46] Moreover, they show that the interaction with the substrate leads to a charge redistribution within the BF-DPB molecule, see Figure S6 (Supporting Information), affecting presumably the molecular orbitals (HOMO and LUMO) and thus the electronic states. The resulting change of the energy levels of electronic states supports the hypothesis that molecule-substrate interaction enhances intersystem crossing of BF-DPB.

3. Conclusion

We used high-resolution scanning probe microscopy to directly image the molecular assembly of vacuum-deposited BPyMPM and BF-DPB films on various substrates and to gain insights into the intermolecular interactions responsible for the different assemblies.

The results show that B4PyMPM molecules form self-assemblies on both Au(111) and Cu(111), which are caused by C—H...N hydrogen bonds and metal coordination bonds, respectively. B2PyMPM molecules, on the other hand, only form disordered structures on both substrates. This difference in molecular assembly is caused exclusively by the different position of the nitrogen atoms in their peripheral pyridine rings.

BF-DPB molecules form two types of self-assemblies, which are determined by van der Waals interaction. On the substrate, the optical properties of BF-DPB are drastically changed compared to the bulk, probably due to an enhanced intersystem crossing.

At domain boundaries between BF-DPB and B4PyMPM, the molecules show a considerable disorder without any binding sites between BF-DPB and B4PyMPM. The agglomerates that form at the boundaries exhibit a higher energy gap than the ordered domains. Previously proposed models for exciton and CT state dissociation and subsequent free carrier generation have postulated the importance of disordered phases in the dissociation process: The energy offset between the more disordered interface and the more ordered bulk drives the charge carriers to the neat, more ordered phases, away from the interface.[47] Free charges then travel in the higher mobility bulk regions of the neat phases to the electrodes. This demonstrates the crucial correlation of molecular order and electro-optical properties in organic functional layers.

Furthermore, we find that the agglomeration on passivation layers such as NaCl or metal oxide as well as in the second molecular layer is strongly suppressed and shows a significant

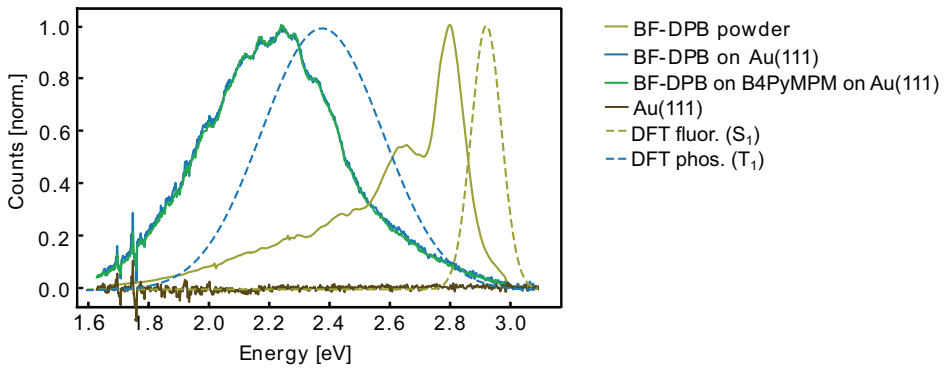

Figure 9. Measurements of a BF-DPB powder, BF-DPB on a Au(111) substrate, BF-DPB on B4PyMPM on top of a Au(111) substrate, and pure Au(111) as well as DFT calculated fluorescence (emission from the S_1 singlet state) and phosphorescence spectra (emission from the T_1 triplet state) in the gas phase. For the sample of BF-DPB on Au(111), BF-DPB was evaporated for 15 min. For the sample with an additional B4PyMPM layer, B4PyMPM was evaporated on Au(111) for 40 min, then BF-DPB for 15 min.

reduction in the 2D character of the structures. Overall, the choice of substrate thus has a major effect on the molecular assembly and the resulting functional properties of BPyMPM and BF-DPB. In general, this must be taken into consideration when developing tailored donor-acceptor systems and suitable contact layers for organic optoelectronic devices.

4. Experimental Section

The STM measurements were performed with a low-temperature scanning probe system (LT-STM/AFM, Scienta Omicron, MATRIX SPM control system) at ultra-high vacuum conditions with a base pressure below 4×10^{-11} mbar. Before the measurement, the samples were cooled down to liquid-nitrogen temperature (~78 K). Only the measurements shown in Figure S4 (Supporting Information) were carried out at liquid-helium temperature (~4 K).

Two types of scanning tunneling tips were applied. The first one was electrochemically etched from a 0.2 mm thick annealed monocrystalline tungsten wire and used for the measurements shown in Figures 2, 3, 4, and 6; Figures S3 and S4 (Supporting Information). The second tip was made from 0.25 mm thick annealed platinum-iridium wire using the cut-and-pull method and was used for the measurements shown in Figures 5, 7, and 8; Figures S2 and S5 (Supporting Information). Both tips were further formed by tip-sample indentations and voltage pulses on a Au(111) substrate to create a sharp and stable apex.

For sample preparation, Au(111) and Cu(111) Mateck single crystals were cleaned by repeated cycles of Ar+ ion sputtering and subsequent annealing at up to 600 K. The molecules were purchased from Sigma–Aldrich (B4PyMPM and B3PyMPM), from Lumtec (B2PyMPM) and from AA Blocks (BF-DPB). They were deposited by thermal evaporation using a kentax evaporator with quartz crucibles, if not noted otherwise. During evaporation, the substrates were always kept at room temperature. B4PyMPM was evaporated at 245 °C to 250 °C, BF-DPB at 220 °C, B3PyMPM at 215 °C, and B2PyMPM at 205 °C to 210 °C. The evaporation times are noted in the figure captions.

NaCl was evaporated at 600°C for 20s while the substrates were kept at room temperature. Oxidation of the Cu(111) substrates was achieved by dosing O_2 with a pressure of 10^{-6} mbar for 10 min while the substrates were kept at 220 °C.

For the STS measurements, the tip position was set with voltage and tunneling current setpoints of −2.3 V and 7 pA. The feedback loop was then deactivated and the bias voltage was swept from −2.3 V to 2.8 V or 3.1 V in case of the BF-DPB self-assembly and the agglomerate, respectively. Each current-voltage curve consists of 60 measurement points, with a measurement time of 50 ms per point, resulting in a total duration of 3 s per curve. The dI/dV spectra were obtained by numerical differentiation of the current-voltage curves and subsequent averaging over several spectra for both the self-assembly and the agglomerate.

The BF-DPB powder sample was prepared by depositing a thin layer of the powder on a Si/SiO_2 substrate with a SiO_2 thickness of 80 nm. To measure the photoluminescence, a homebuilt microscope equipped with a small vacuum chamber was used. While transferring the samples into this chamber, they were in ambient atmosphere for 1–2 min. The samples were excited with a pulsed 375 nm PicoQuant diode laser (LDH-P-C-375) and the emission was detected using an Andor Shamrock 303i spectrograph with a Scientific CMOS camera (Andor Neo) attached. To remove stray light of the laser, the emission was cut off at 409 nm using a Semrock BrightLine HC 409/LP long-pass filter. To focus onto the sample and to collect the photoluminescence in reflection geometry, a 10x objective lens with a numerical aperture of 0.3 (Nikon TU Plan Fluor 10x) was used. Hence, the emitted light was collected from an area with a diameter of 1 µm.

Supporting Information

Supporting Information is available from the Wiley Online Library or from the author.

Acknowledgements

This work was funded by the Deutsche Forschungsgemeinschaft (DFG, German Research Foundation) through project 519972808.

Open access funding enabled and organized by Projekt DEAL.

Conflict of Interest

The authors declare no conflict of interest.

Data Availability Statement

The data that support the findings of this study are available from the corresponding author upon reasonable request.

Keywords

B4PyMPM, BF-DPB, hydrogen bonds, metal coordination bonds, molecular assembly, organic solar cells, scanning tunneling microscopy

Received: October 24, 2024
Revised: January 13, 2025
Published online: February 5, 2025

[1] H. Wu, H. Fan, S. Xu, L. Ye, Y. Guo, Y. Yi, H. Ade, X. Zhu, *Small* **2019**, *15*, 1804271.
[2] F. Zhao, C. Wang, X. Zhan, *Adv. Energy Mater.* **2018**, *8*, 1703147.
[3] W. Li, M. Chen, J. Cai, E. L. Spooner, H. Zhang, R. S. Gurney, D. Liu, Z. Xiao, D. G. Lidzey, L. Ding, T. Wang, *Joule* **2019**, *3*, 819.
[4] H. Wu, H. Fan, W. Liu, S. Chen, C. Yang, L. Ye, H. Ade, X. Zhu, *Small* **2019**, *15*, 1902656.
[5] H. Chen, D. Hu, Q. Yang, J. Gao, J. Fu, K. Yang, H. He, S. Chen, Z. Kan, T. Duan, C. Yang, J. Ouyang, Z. Xiao, K. Sun, S. Lu, *Joule* **2019**, *3*, 3034.
[6] S. Chen, J. Ye, Q. Yang, J. Oh, D. Hu, K. Yang, G. O. Odunmbaku, F. Li, Q. Yu, Z. Kan, Z. Xiao, C. Yang, S. Li, K. Sun, *J. Mater. Chem. A* **2021**, *9*, 2857.
[7] Z. Xiao, T. Duan, H. Chen, K. Sun, S. Lu, *Sol. Energy Mater. Sol. Cells* **2018**, *182*, 1.
[8] W. Gao, R. Ma, T. A. Dela Pe na, C. Yan, H. Li, M. Li, J. Wu, P. Cheng, C. Zhong, Z. Wei, A. Jen, G. Li, *Nat. Commun.* **2024**, *15*, 1946.
[9] Y. Ma, M. Zhang, S. Wan, P. Yin, P. Wang, D. Cai, F. Liu, Q. Zheng, *Joule* **2021**, *5*, 197.
[10] D. Yokoyama, H. Sasabe, Y. Furukawa, C. Adachi, J. Kido, *Adv. Funct. Mater.* **2011**, *21*, 1375.
[11] X. Jia, L. Soprani, G. Londi, S. M. Hosseini, F. Talnack, S. Mannsfeld, S. Shoaee, D. Neher, S. Reineke, L. Muccioli, G. D'Avino, K. Vandewal, D. Beljonne, D. Spoltore, *Mater. Horiz.* **2024**, *11*, 173.
[12] S. Ullbrich, J. Benduhn, X. Jia, V. C. Nikolis, K. Tvingstedt, F. Piersimoni, S. Roland, Y. Liu, J. Wu, A. Fischer, D. Neher, S. Reineke, D. Spoltore, K. Vandewal, *Nat. Mater.* **2019**, *18*, 459.
[13] W. Brütting, *Nat. Mater.* **2019**, *18*, 432.
[14] R. Meerheim, S. Olthof, M. Hermenau, S. Scholz, A. Petrich, N. Tessler, O. Solomeshch, B. Lüssem, M. Riede, K. Leo, *Jpn. J. Appl. Phys.* **2011**, *109*, 103102.
[15] C. Murawski, C. Fuchs, S. Hofmann, K. Leo, M. C. Gather, *Appl. Phys. Lett.* **2014**, *105*, 113303.
[16] R. Meerheim, C. Körner, K. Leo, *Appl. Phys. Lett.* **2014**, *105*, 063306.
[17] M. L. Ball, Q. Burlingame, H. L. Smith, T. Liu, S. R. Parkin, A. Kahn, Y.-L. Loo, *ACS Energy Lett.* **2021**, *7*, 180.

[18] Q. C. Burlingame, X. Liu, M. L. Ball, B. P. Rand, Y.-L. Loo, *Energy Environ. Sci.* **2023**, *16*, 1742.
[19] S.-Q. Sun, H. Liu, D.-D. Feng, C.-C. Huang, T.-T. Wang, W. He, Y.-J. Zhang, W. Luo, Q. Sun, M.-K. Fung, *J. Mater. Chem. C* **2021**, *9*, 14327.
[20] H. Sasabe, D. Tanaka, D. Yokoyama, T. Chiba, Y.-J. Pu, K.-i. Nakayama, M. Yokoyama, J. Kido, *Adv. Funct. Mater.* **2011**, *21*, 336.
[21] I. Caballero-Quintana, O. Amargós-Reyes, J.-L. Maldonado, J. Nicasio-Collazo, D. Romero-Borja, D. Barreiro-Argüelles, G. Molnár, A. Bousseksou, *ACS Appl. Mater. Interfaces* **2020**, *12*, 29520.
[22] I. Caballero-Quintana, J.-L. Maldonado, M.-A. Meneses-Nava, O. Barbosa-García, J. Valenzuela-Benavides, A. Bousseksou, *Adv. Electron. Mater.* **2019**, *5*, 1800499.
[23] K. Maturová, R. A. Janssen, M. Kemerink, *ACS Nano* **2010**, *4*, 1385.
[24] T. Sirtl, S. Schlögl, A. Rastgoo-Lahrood, J. Jelic, S. Neogi, M. Schmittel, W. M. Heckl, K. Reuter, M. Lackinger, *J. Am. Chem. Soc.* **2013**, *135*, 691.
[25] J. V. Barth, J. Weckesser, C. Cai, P. Günter, L. Bürgi, O. Jeandupeux, K. Kern, *Angew. Chem., Int. Ed.* **2000**, *39*, 1230.
[26] G. Pawin, U. Solanki, K.-Y. Kwon, K. L. Wong, X. Lin, T. Jiao, L. Bartels, *J. Am. Chem. Soc.* **2007**, *129*, 12056.
[27] T. Klitsner, R. Becker, J. Vickers, *Phys. Rev. B* **1990**, *41*, 3837.
[28] F. Gao, O. Inganäs, *Phys. Chem. Chem. Phys.* **2014**, *16*, 20291.
[29] S. Shoaee, S. Subramaniyan, H. Xin, C. Keiderling, P. S. Tuladhar, F. Jamieson, S. A. Jenekhe, J. R. Durrant, *Adv. Funct. Mater.* **2013**, *23*, 3286.
[30] S.-i. Natsuda, T. Saito, R. Shirouchi, Y. Sakamoto, T. Takeyama, Y. Tamai, H. Ohkita, *Energy Environ. Sci.* **2022**, *15*, 1545.
[31] O. V. Mikhnenko, P. W. Blom, T.-Q. Nguyen, *Energy Environ. Sci.* **2015**, *8*, 1867.
[32] W. Tress, *Organic solar cells*, Springer, **2014**.
[33] J. Gupta, C. Nunes, S. Vyas, S. Jonnalagadda, *J. Phys. Chem. B* **2011**, *115*, 2014.
[34] B. Hammer, J. K. Nørskov, *Nature* **1995**, *376*, 238.
[35] T. Wang, J. Zhu, *Surf. Sci. Rep.* **2019**, *74*, 97.
[36] B. S. Lammers, N. López-Salas, J. S. Siena, H. Mirhosseini, D. Yesilpinar, J. Heske, T. D. Kühne, H. Fuchs, M. Antonietti, H. Mönig, *ACS Nano* **2022**, *16*, 14284.
[37] L. Bartels, *Nat. Chem.* **2010**, *2*, 87.
[38] S. L. Tait, A. Langner, N. Lin, S. Stepanow, C. Rajadurai, M. Ruben, K. Kern, *J. Phys. Chem. C* **2007**, *111*, 10982.
[39] J. V. Barth, *Annu. Rev. Phys.* **2007**, *58*, 375.
[40] F. J. Giessibl, *Rev. Sci. Instrum.* **2019**, *90*, 1.
[41] B. S. Lammers, D. Yesilpinar, A. Timmer, Z. Hu, W. Ji, S. Amirjalayer, H. Fuchs, H. Mönig, *Nanoscale* **2021**, *13*, 13617.
[42] J. Repp, G. Meyer, *Appl. Phys. A* **2006**, *85*, 399.
[43] C. Barth, M. Gingras, A. S. Foster, A. Gulans, G. Félix, T. Hynninen, R. Peresutti, C. R. Henry, *Adv. Mater.* **2012**, *24*, 3228.
[44] Q. Xu, F. Wang, Z. Tan, L. Li, S. Li, X. Hou, G. Sun, X. Tu, J. Hou, Y. Li, *ACS Appl. Mater. Interfaces* **2013**, *5*, 10658.
[45] G. Wang, A. Rühling, S. Amirjalayer, M. Knor, J. B. Ernst, C. Richter, H.-J. Gao, A. Timmer, H.-Y. Gao, N. L. Doltsinis, F. Glorius, H. Fuchs, *Nat. Chem.* **2017**, *9*, 152.
[46] A. Timmer, H. Mönig, M. Uphoff, O. Díaz Arado, S. Amirjalayer, H. Fuchs, *Nano Lett.* **2018**, *18*, 4123.
[47] F. C. Jamieson, E. B. Domingo, T. McCarthy-Ward, M. Heeney, N. Stingelin, J. R. Durrant, *Chem. Sci.* **2012**, *3*, 485.